Taylor & Francis
Taylor & Francis Group

Radiofrequency ablation of hepatic tumors: simulation, planning, and contribution of virtual reality and haptics

CAROLINE VILLARD†*, LUC SOLER‡ and AFSHIN GANGI¶

†LSIIT boulevard Sebastien Brant, Illkirch, F67400, France
‡IRCAD, 1, place de l'Hôpital, Strasbourg, F67091, France
¶Hôpital Civil–Radiologie B 1, place de l'Hôpital, Strasbourg, F67091, France

For radiofrequency ablation (RFA) of liver tumors, evaluation of vascular architecture, post-RFA necrosis prediction, and the choice of a suitable needle placement strategy using conventional radiological techniques remain difficult. In an attempt to enhance the safety of RFA, a 3D simulator, treatment planning, and training tool, that simulates the insertion of the needle, the necrosis of the treated area, and proposes an optimal needle placement, has been developed. The 3D scenes are automatically reconstructed from enhanced spiral CT scans. The simulator takes into account the cooling effect of local vessels greater than 3 mm in diameter, making necrosis shapes more realistic. Optimal needle positioning can be automatically generated by the software to produce complete destruction of the tumor, with maximum respect of the healthy liver and of all major structures to avoid. We also studied how the use of virtual reality and haptic devices are valuable to make simulation and training realistic and effective.

Keywords: Minimally invasive surgery; Treatment simulation and planning; Computer-assisted surgery; 3D visualization; Virtual reality; Haptic interfaces

1. Introduction

Over the past 10 years, several minimally invasive techniques for liver tumor ablation have emerged thanks to recent advancements in medical imaging. Among them, percutaneous thermal ablation has been studied in different forms, such as microwave, laser, ultrasound, cryotherapy, and radiofrequency (RF) that appears to be the easiest, safest and most predictable (McGahan and Dodd 2001).

Radiofrequency ablation (RFA) of a tumor consists in an ionic agitation generated by the principle of a microwave located at the tip of a needle-like probe, producing a tumor coagulative necrosis when heated enough. To treat a large zone, the probe may be positioned several times. Radiologists burn the whole tumor volume with a 0.5–1 cm security margin (Cady *et al.* 1998), which is mandatory to prevent local recurrence of a tumor after treatment, and to reduce the effects of a possible inaccuracy of needle placement.

The success of such a percutaneous treatment closely depends on the choice of secure probe trajectories, the destruction of a maximum number of cancerous cells, and a minimum amount of affected healthy tissues. Unfortunately, treatment planning is quite difficult for a radiologist who can only rely on 2D scanner slices.

New techniques of scanner image reconstruction allow a more intuitive 3D visualization of the patient's anatomy (Soler *et al.* 2001), that makes the simulation of needle placement possible. The expected follow-ups of this functionality are both the visualization of the necrosis of treated zones, and the automatic planning of needle trajectories that would optimize the three above criteria. Another expected point is simulation for training. With the recent emergence of virtual reality techniques and the development of haptic devices, a better realism is possible.

In this paper, after a state of the art, we explain how we simulate the necrosis of the treated area. Then, we show how to automatically compute optimal needle positions. Before concluding, we describe the experimentations we performed with virtual reality and haptic devices to enhance the realism of the simulation, and we discuss the future improvements we plan to add.

---

*Corresponding author. E-mail: villard@lsiit.u-strasbg.fr

2. State of the art

For this kind of work about radiofrequency simulation and planning, the state of the art can be divided in two main sources: medical studies, that bring us information on the recent discoveries about the treatment technique and the different factors involved, and computer science works by other teams that examined different types of computer-aided simulations.

2.1 Medical studies

In order to simulate accurately the ablation of a tumor using percutaneous RF, we first have to know exactly what are: the effect of the treatment in terms of lesion size and shape, the effect in specific cases due to treatment location or to a possible pathology, and all factors influencing the success of the treatment. A lot of studies have been done to report the discoveries in this field (McGahan and Dodd 2001).

Recent works, not only concerning liver tumors, but also other RF applications like cardiac arrhythmias, prostate or brain tumors, bring us information about factors influencing lesion size and shape, that have to be taken into account to make an accurate prediction for our simulation. Several kinds of factors are involved: device- or strategy-dependent, anatomic, or pathologic factors.

We know that the shape of the lesion depends on the type and design of probe, and its size varies according to the power supplied by the associated generator (Goldberg *et al.* 2000, Goldberg 2001, de Baere *et al.* 2001). The shape of a lesion is generally spherical in the case of an expandable needle, or more ellipsoidal in the case of non-expandable systems. Some studies tried to find ways to increase the size of the necrosis, in order to be able to treat larger tumors. The design of more sophisticated probes (cooled probes, clusters of probes) helped in treating larger areas. *In vivo* studies on pig livers were reported by Pereira *et al.* (2004), that give an idea of lesions sizes and shapes for 4 different devices.

Some other factors can affect the theoretical necrosis shape. It seems that the shape of lesions is not the same in the case of cirrhotic/non-cirrhotic livers (Livraghi *et al.* 1999). A principal source of heat loss is also vascular flow, that can induce a deformation of the necrosis zone. The *heat-sink* effect caused by blood flow inside vessel network prevent from a complete necrosis. The vessels involved in this phenomenon seem to be the largest ones (diameter larger than 3 mm de Baere *et al.* 2001), as smallest ones are thrombosed. Strategies such as blood supply occlusion allow to enlarge lesions, that are not disturbed by the heat-sink effect anymore (Rossi *et al.* 2000, Yamasaki *et al.* 2002, de Baere *et al.* 2002).

Finally, some strategies using overlapping ablations allow to treat tumors that could not have been treated with a single needle insertion (Wood *et al.* 2000, Dodd *et al.* 2001, Chen *et al.* 2004).

2.2 Computer-aided simulation and planning

One of the first interests of computer-aided simulation and planing is the ability to see a 3D view of the patient who will receive the treatment. Antoch *et al.* 2002 underlined in the importance of a volumic view of the patient in the domain of RF treatment, as the success of RF ablation is dependent on an accurate positioning of the ablation probe.

On a technical point of view, quite few studies have been carried out on treatment simulation in the domain of RF. Some of them concerned other minimally invasive treatments such as cryotherapy (Rewcastle *et al.* 2001), and allowed to simulate iceball growth. Others were centered on finite elements modeling of RF treatment and did not seem to be fast, that is an essential point for a real-time simulation, and were often focused on heart diseases (Jain and Wolf 2000, Gopalakrishnan 2002, Tungjitku-solmun *et al.* 2002).

Butz *et al.* 2000 proposed a very interesting cryotherapy simulator and planner, included in *3D-Slicer*, that can also be extended to one type of RF probe. However, it can only compute the best positioning of cryoprobes within a predefined window of the body, and does not take into account the presence of surrounding organs.

To our knowledge, there were no works reported on the use of virtual reality 3D display and force feedback devices for the simulation of RFA treatment. However, we think that these techniques would be appreciable to enhance the realism of a simulation, especially for training purposes.

Compared to previous works, we propose a real-time simulation and quite fast planning tool, dedicated to RFA of hepatic tumors, that allies performance and realism, with the help of virtual reality and haptic devices.

3. Visualizing the patient and simulating the necrosis zone

Our researches started with the expression of a need from radiologists to visualize more easily information about their patients, their anatomy and pathologies, and to be able to simulate accurately and realistically RF treatment before operating. Our tool, called *RF-Sim*, responds to these needs by linking 3D reconstruction of slices from an enhanced spiral CT scan (Soler *et al.* 2001), 3D view of the patient, and virtual probe placement simulation and computation.

From enhanced spiral CT scans with 2 mm cuts, three dimensional (3D) reconstruction of patients with liver metastases are generated using a SGI octane2 under Unix with a R12000 processor at 400 MHz and 1Go of RAM. The dedicated software detects, delineates and reconstructs automatically their liver, pathologies, and surrounding organs. It produces realistic and manipulable 3D scenes representing the anatomy of the patients, in which it is possible to navigate easily, and to hide or show a selection of organs.

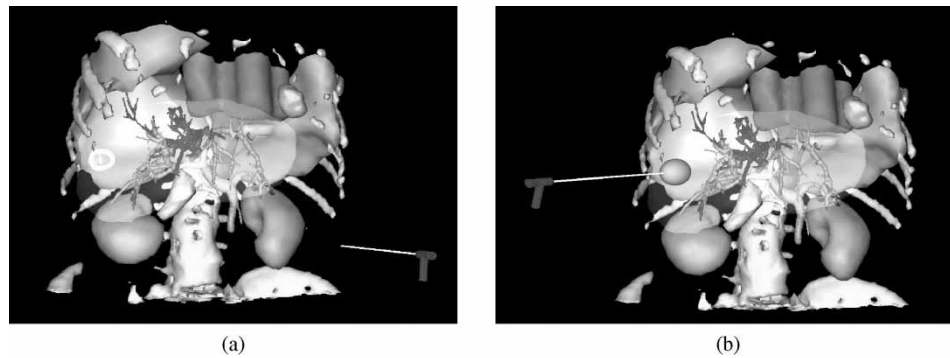(a)   (b)

Figure 1.   A classic 3d scene with *RF-Sim*. (a) patient's organs and pathology, and an additional virtual probe (b) estimated necrosis zone for a specific needle placement.

Then, simulations of RFA can be performed, based upon the characteristics of the Berchtold HITT needle. A user of the simulator can add virtual probes into the 3D scene of the patient's organs, as shown on figure 1, and then freely translate and rotate them. During a simulation, for each attempt of needle placement, the corresponding lesion zone is estimated and simulated as a simple meshed spheroid representing the 60°C isosurface.

The simulator is also able to take into account the cooling effect of local vessels greater than 3 mm in diameter. To simulate this heat-sink effect induced by the vessels, we update the shape of the ellipsoid by repulsing some of its vertices away from the vessel shapes, towards the inside of the ellipsoid.

To represent the lesion zone, we did not choose a physics-based model, generally computed thanks to finite element methods, because it would not have fitted our real-time criterion, for the simulator part. Choosing to represent the lesion by its 60°C isosurface allows us to perform a real-time approximation of the zone and of the deformation caused by the heat-sink effect, precise enough to be realistic, but simplified enough to be updated as fast as the user moves the needle.

Our deformation method, uses a voxel representation of the vessel network and a voxel-based algorithm taking advantage of mathematical morphology techniques (Villard *et al.* 2003). Large vessels cool their surrounding area and remain unchanged after the treatment, whereas small vessels are considered as being burnt. To reproduce this effect, we perform a sufficient number of erosions on the voxel shape to make small vessels disappear, only thinning large ones. The number of erosions is determined by the size of small vessels to eliminate ($\varnothing < 2-3$ mm) and the resolution of the voxel mask. The average resolution of the masks we currently use is $0.6 \times 0.6 \times 0.6$ mm, so we perform 2 erosions in order to eliminate vessels having a radius < 1.2 mm, i.e. a diameter < 2.4 mm. Performing 3 erosions would eliminate too many vessels ($\varnothing < 3.6$) and performing only 1 erosion would miss out on some vessels ($1.2 < \varnothing < 2.4$). Then, the same number of dilations brings large vessels to their initial thickness. In a second step, we perform some more dilations, in order to increase thickness of large vessels. Indeed, the "heat-sink" effect also cools the area surrounding the vessel, so the zone has to be extended to include this area. We obtain a deformation zone that incorporates large vessels and their neighborhood, and that excludes small vessels.

An example of necrosis shape deformation is shown on figure 2. The deformation is computed in real-time while the user moves a needle or controls a lesion growth, to allow updates while needle is being adjusted. This is important as we want our prototype to be able to be run on every common laptop, to be brought in the operating room, and to be used live on location. This allows to observe whether the considered needle placement strategy would burn the whole cancerous zone or not.

Beside this real-time treatment simulator, the prototype proposes another functionality to help radiologists in their treatment planning, having as an objective to be fast (a few minutes at worst) but without sacrifying precision. This functionality, that we will detail in the next section, is based on a method that computes the optimal placement for one or more needle probes in order to burn a maximum volume of the tumor and its margin, while preserving healthy tissue.
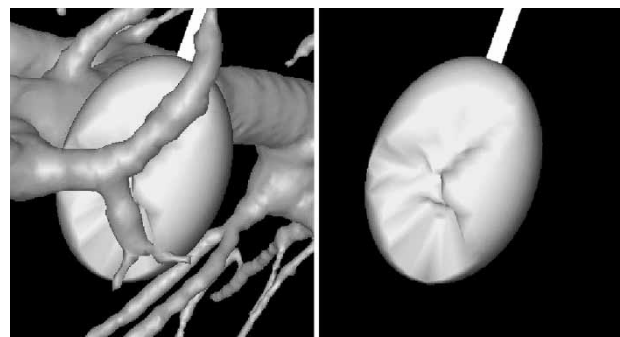

Figure 2.   Example of deformation of the necrosis zone due to the presence of vessels. On the right, vessels are hidden to see more clearly the deformation.

4. Automatic positioning of the needle for treatment planning

4.1 Optimal placement for a single needle introduction

First, let us examine the case where there is only one tumor, small enough to be treated by a single needle insertion, and where we do not take into account surrounding organs. Then, the problem is reduced to a simpler one: how to find the minimal spheroidal lesion containing the tumor and its margin? This is a classical problem, which can be solved using various possible algorithms of function minimization. If we can determine a function finding the smallest spheroid covering the tumor shape knowing a fixed needle axis, then we can try to minimize the value returned by the first function by gradually moving the needle axis, making it quickly converge to a stable minimum. Therefore, our first step is to precisely define the function to minimize.

4.1.1 First step: volume minimization with fixed needle axis.

Let us notice that the lesion shape we consider has particular properties, because of its generation from microholes located at the needle tip, that allow us to make a simplification in the evaluation of its volume. It is a prolate *spheroid*, whose major axis is the needle, i.e. an ellipsoid where radii r_1, r_2, and r_3 verify: $r_3 = r_1$ and $r_2 = k \cdot r_1$, and k is the ratio: {major axis size}/{minor axis size}. Therefore, the volume of such a spheroid being $V = (4/3)\pi r_1 r_2 r_3$, it can be rewritten as $V = (4/3)\pi k r_1^3$. In this particular case of a single lesion, we consider this simplification: including the margin in the lesion will be seen as including all margin mesh vertices inside the spheroid. Now, given the center C of the ellipsoid and the orientation of its axes, and given the tumor margin mesh, we can define a function that finds the minimum r_1 such that every vertex of the mesh is inside the spheroid. This is done by initializing r_1 to a small value, and then for each vertex of the mesh, increasing r_1 minimally if the vertex was outside so that it comes inside.

A point $p(x, y, z)$ is inside the spheroid if and only if

$$\frac{x^2}{r_1^2} + \frac{y^2}{k^2 r_1^2} + \frac{z^2}{r_1^2} < 1$$

So the algorithm is the following. We initialize r_1 to
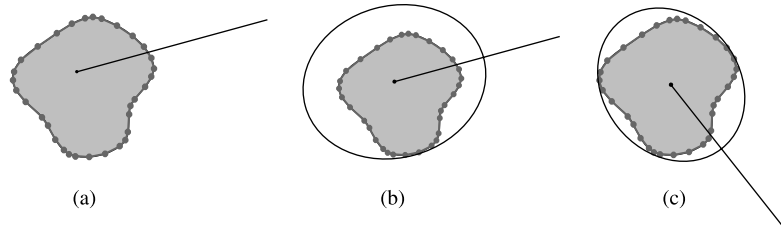
$$\sqrt{x_0^2 + \frac{y_0^2}{k^2} + z_0^2}$$

Considering that the first point $p_0(x_0, y_0, z_0)$ of the mesh is on the initial spheroid. Then, for each vertex p_i of the margin mesh, we test if it is inside the current spheroid or not: if

$$\frac{x_i^2}{r_1^2} + \frac{y_i^2}{k^2 r_1^2} + \frac{z_i^2}{r_1^2} > 1$$

we replace r_1 by

$$r_1' = \sqrt{x_i^2 + \frac{y_i^2}{k^2} + z_i^2}$$

At the end, we obtain the minimal particular spheroid containing all vertices, according to the given center and orientations. This minimal covering volume function will be called *ComputeBestSize*, and be used as our function to minimize. Figure 3(a) and (b) illustrate the application of this algorithm on a 2D example.

4.1.2 Second step: finding the best position for the needle.

Now that we can compute the best bounding spheroid around a tumor margin knowing its center and orientation, we have to find the best center and orientation minimizing this bounding volume. We can use one of the classic minimization algorithms (using no derivatives), such as downhill simplex or Powell's direction set methods in multidimensions, or simulated annealing method (Press *et al.* 2002).

We consider *ComputeBestSize* as taking 6 parameters: 3 center coordinates and 3 orientations of the spheroid. Therefore, we use minimization methods in $n = 6$ dimensions. Downhill simplex method (DH) has to start with an initial simplex X, i.e. $n + 1 = 7$ vertices. We use as parameters the initial center $X_0 = (0,0,0,0,0,0)$, and a weighting of the 6 unit vectors $X_1 \ldots X_6$, as well as a tolerance *tol* determining the termination criterion. After a few iterations, the initial simplex has contracted itself into a valley floor, and is returned by the algorithm: $(X_0(0), X_0(1), X_0(2))$ is an approximation of the best center, and $X_0(3)$, $X_0(4)$, and $X_0(5)$ are approximations of the best orientation coordinates of the spheroid. We can see on figure 3(c) the minimal fitting ellipse that can be found using this method on the previous 2D example.

In a similar way, Powell's direction set method (PW) needs an initial point $X_0 = (0,0,0,0,0,0)$, a set of

(a)   (b)   (c)

Figure 3. (a) and (b): fitting an ellipse with fixed center and orientation around a 2D shape; (c): fitting a minimal ellipse around a 2D shape.

initial directions $(X_1 \ldots X_6)$, and a tolerance *tol*. After some successive line minimizations along coordinate directions, it returns the best point and orientation as X_0 when there is a failure to decrease the function value by more than *tol*. However, both methods have the drawback to be sensitive to local minima. Because of that, we improve the result accuracy by first bringing roughly the needle at an initial position, estimated to be close to the best position, or at least by placing the needle tip inside tumor margin.

To avoid this phenomenon, we tried to use the simulated annealing algorithm, that is less subject to local minima. It is based on random steps, that become smaller and smaller as a factor T decreases. It allows jumps over local hills to find possibly better valleys. However, in our case this method did not give as good results as expected, because of a very long execution time, and because the involved parameters are very difficult to adjust. It would be too long to find the parameters that fit each new tumor shape, each new patient case.

Results of all three methods are exposed in Section 5.

4.2 *Larger tumors treatment with several optimal placements of a needle sequentially*

As we said earlier, until now there is a maximum size for lesions because of the limits of RF technology. This limit makes it necessary to itemize large margin meshes in smaller sets that could be covered with smaller overlapping spheroids. Let us precise that the term of overlapping spheroid we will use in this paper does not mean that several needles are inserted to treat simultaneously several regions. It means that several insertions are performed sequentially with a needle, each separate treatment burning a different area, one by one. This implies that there is no interaction or energy transfer between the different parts of the process, so we can still use spheroids, overlapping to represent the global burnt region.

4.2.1 Using voxel representation of tumors. When using several spheroids (several needle insertions) to cover a mesh, we can not simplify anymore by only including all mesh's vertices, because in some cases a consequential portion of the mesh volume can be forgotten, as shown on figure 4(a) in a 2D example.
Therefore, we decided to include the whole voxel representation, as illustrated on figure 4(b), to ensure a total burning of the shape. However, we will still keep the meshed margin for display.

The voxel representation of the security margin is quite easy to obtain, as we already have the tumor voxel representation, that was directly reconstructed from the scans. We only have to perform an enlargement on the tumor voxel shape to obtain the margin voxel shape. To do this, we first perform a *distance transform* on the voxels, to produce a *distance map*, i.e. an assignation of a scalar d to each point of the image, d representing the distance from
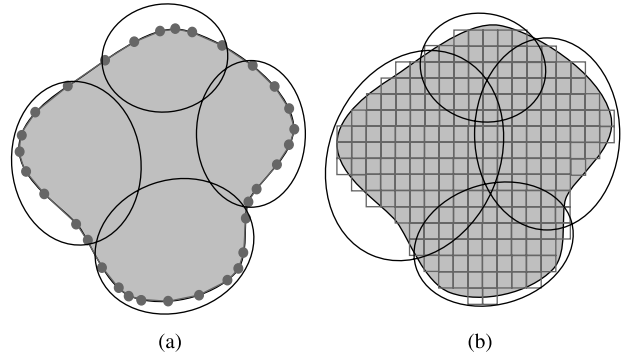

Figure 4. Trying to cover a 2D shape with 4 ellipses. (a) using mesh representation (b) using voxel representation.

the tumor (Meijster *et al.* 2000). Then, we threshold the distance map, according to a margin size s, to add to tumor voxel shape every voxel being at a distance $d < s$ from it. For now, we consider $s = 5$ mm as being the most commonly used margin size, but we allow the user to modify (increase or decrease) this size in a near-real-time operation, simply thresholding the distance with a different value. However, in most cases, this treatment is done once, when the data are loaded.

This modification of the type of data (voxels instead of vertices) does not affect much computation time, because we observed that in most cases of tumors we were dealing with, the automatic reconstruction provided us a mesh having a number of vertices quite similar to the original number of voxels

4.2.2 Modification of *ComputeBestSize*. According to this new representation and the addition of more needles, we modified *ComputeBestSize* to produce a new algorithm called *ComputeBestSizeMoreSpheroids*. Recall that the inputs are fixed needle positions, and that our aim is to find the minimum size for each lesion in order to cover the whole voxel shape.
We first cut the voxel shape in smaller subsets that we will be able to include in lesions of a reasonable size. We distribute the voxels in the subsets, called *influence zones*, according to their distance to needle tips: a point in the tissue will be burnt by the nearest needle. We show an example of the result in 2D on figure 5(a).

Then, when the distribution is done, we perform the previous algorithm for each needle and its subset, to find the smallest covering spheroid (figure 5(b)). The returned volume (to minimize) is the sum of the volumes of the spheroids.

To find the best positions for the needles, we perform one of the optimization algorithms, simply passing as parameters all tip positions and needle orientations, and having the new *ComputeBestSizeMoreSpheroids* algorithm as a value to minimize. After a moment, a convergence, determined by the given tolerance *tol*, fixes all needle positions and orientations.
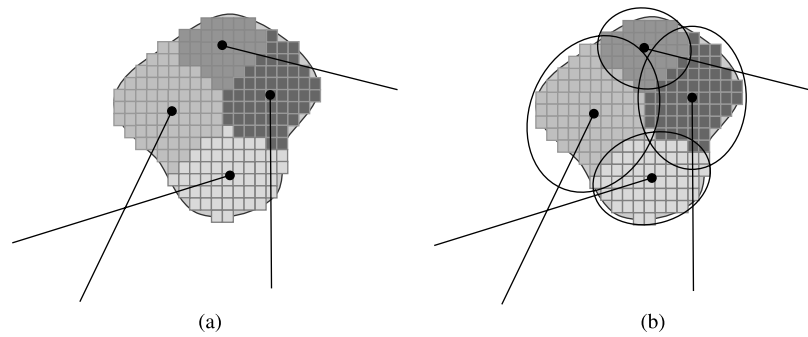
Figure 5.   Division of a voxel shape in 4 subsets. (a) subsets using distance from needle tips (b) smallest ellipsoids for each subset.

4.3 Avoiding vital structures

Another important criterion for a successful RF treatment is the total safety of the procedure. The choice of secure trajectories for needle insertions is an essential point. That is why we decided to include a collision detection system that allows extrahepatic and intrahepatic vital structures avoidance.

In order to take into account surrounding vital or rigid organs, we have to control the optimization process, by preventing the research of the minimum to converge to an unauthorized trajectory. A trajectory is acceptable only if it intersects skin, liver, and a tumor and its margin. All trajectories intersecting other organs are forbidden, either because a needle insertion through them would be fatal, or cause serious damages (heart, portal vein, etc.), or because their physical properties do not allow a needle to go through (bones). Therefore, for each considered trajectory, we need to compute its intersections with the patients organs.

To compute intersections, we use an algorithm based on the voxel representation of the organs. We construct a voxel set from all vital organs that have to be avoided (i.e. all organs except skin, liver, tumor and margin). Then this set is enlarged of 5 mm, using mathematic morphology techniques, in order to let a safety margin around it to avoid trajectories involving major risks. This set is then used as a prohibited area, through which the needle cannot pass. For each considered trajectory, we compute the intersection with this enlarged set.

Then, we use the result of the collisions detection as a condition to weight the volume returned by *ComputeBestSizeMoreSpheroids*. If the trajectory is wrong, this function will return such a high volume that the optimization function will necessarily decide to give up progression in this direction and search for a more secure path.

Practically speaking, if the needle, for the lesion of which we are going to compute the best size, is going to cross a forbidden organ, then we do not perform the best volume computation, and we place instead as a volume a very high value, prohibitive enough for the optimization process. That way, we save time as many of the candidate trajectories will not need a fitting computation, and the time used to compute intersections will be more or less compensated.

5. Experimentation data and results

5.1 Choice of a minimization method

We present on figure 6, a comparison between results obtained with both methods and different precisions, on a set of 12 patients having a single small liver tumor. All patients' data came from the Strasbourg Civil Hospital and were performed within a preoperative framework. For each case, we launched the method twice.

We chose to compare Downhill simplex (DH) and Powell's direction set (PW) methods with the respective precisions 10^{-3} and 10^{-4} for the first, and 10^{-2} and 10^{-1} for the second, because of their good relevance in terms of ratio *quality of result/execution time*. For both methods, lower or greater precisions gave unacceptable poor quality results or long execution times. On both histograms, whatever the precision, DH method gives better results in almost all cases.

For small tumors, both methods give quite similar volumes. For larger tumors, the difference between volumes is more noticeable, and DH method is better than PW. The average difference between volumes is 2.124 mL, but this is mainly caused by the peak of case 7. If we eliminate lowest and largest cases to avoid exceptional values, the average difference becomes 0.780 ml, and represents an average of 4.53% of the minimum volume (nearly 46% in the worst case).

DH method is also the fastest, especially for large tumors. In 66% of cases, even the slowest DH (10^{-4}) is faster than the fastest PW (10^{-1}). Regarding volume and time performances, DH method being the most interesting, we chose to give preference to DH method, and mainly use it in our further works.

5.2 Needle placement prediction efficiency

A first set of experiments were carried out on 12 patient cases with liver metastases, whose CT scans were provided by our collaborators at the Strasbourg Civil Hospital. Among these cases, 8 had small single tumors (< 10 ml), 1 had a large single tumor needing 2 needles, and 3 had multiple tumors (2,3, and 6 tumors/case).
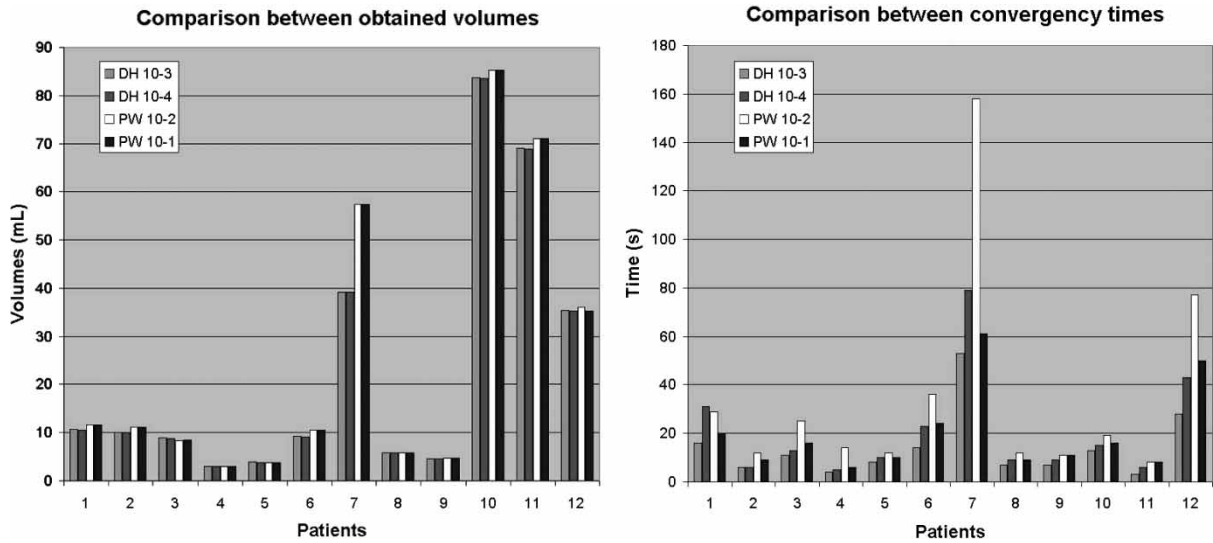
Figure 6. Comparison between 2 minimization methods with different precisions: results in terms of time and obtained volumes. For each patient, the first two sticks are DH method, the 3rd and 4th are PW method.

Multiple tumors are considered as one with several connected components, each of them being treated by their nearest needle.

First, automated reconstruction of all patients organs were successfully achieved from enhanced spiral CT scans with 2 mm cuts. Then, an optimal needle(s) placement was obtained in each case, that was confirmed by expert radiologists. Table 1 summarizes the volumes of predicted lesions compared to volumes to burn.

These experiments show an efficiency above 59.1% (of cancerous cells inside burnt zone), with an average of 73%. Related to the various shapes that tumors can have (tumors never fit exactly an ellipsoid), this can be considered as a good result. Some percentages are not filled because the volume of lesions union has not yet been implemented. Figure 7 shows a possible covering of a tumor with 2 minimal lesions, whose placements were found automatically by our prototype.

From the point of view of process duration, obviously the minimization process takes more time as the number of necessary needles increases, and as the size of the tumor is larger (has a great number of voxels). It starts from 1 second (for the smallest tumor of case 4, with an Athlon XP 1800 + , 512 Mo RAM), and reaches 6 minutes for the most complicated case (#11). For treatment planning, we were not seeking for real time, but our objective was to provide to the surgeon an answer within a reasonable time (a few minutes), that seems to be the case. But we conclude that, if precision seems to be satisfactory, it would be appreciable to find a less time-consuming optimization of the algorithm. Nevertheless, our method is still relatively fast compared to the few known methods using finite elements (Butz *et al.* 2000).

We are currently waiting for extra data to perform our second set of validation experiments, that would allow us to compare the simulated ablation zones to actual ablation zones based on post-ablation CT scans. It will consist in a preoperative automatic treatment planning, and then a comparison *a posteriori*, in terms of efficiency and accuracy, with the effective treatment that was performed.

Table 1. Resulting volumes of minimizations (mL).

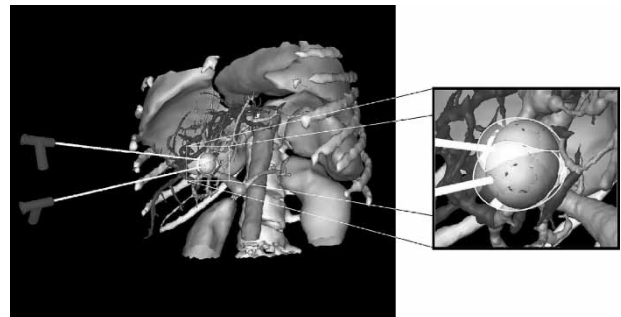| case nb	tumor(s) Nb	tumor(s) volume	lesion(s) nb	lesion(s) volume(s)	effic. of burn
1	1	7.4	1	10.6	69.8%
2	1	6.5	1	10.1	64.3%
3	1	5.2	1	8.8	59.1%
4	1	2.1	1	2.9	72.4%
5	1	3.1	1	3.8	81.6%
6	1	7.1	1	9.2	77.2%
7	1	4.1	1	5.8	70.7%
8	1	3.7	1	4.5	82.2%
9	1	18.7	2	19.9, 17.6	*n.c.*
10	2	6.9	2	3.4, 6.7	68.3%
11	3	48.6	5	13.9, 20.1, 27.7, 24.4, 14.7	*n.c.*
12	6	14.4	6	2.8, 2, 2.1, 2.3, 5.5, 2.3	84.7%

Figure 7. Minimization of the burning zone using 2 overlapping spheroids.

5.3 *Discussion*

Now let us examine a few points. First, the collision detection to avoid perforation of other organs is a plus of our system, but may sometimes become a too strong constraint. If the user first places the needle at an approximative position located in a very narrow path through organs, and then launches the optimization process, it may sometimes prevent the process to find a good solution that would be located outside this path, because the converging movements of the needle cannot pass through the prohibited area. It will cause the process to find the best placement within this narrow path. For now, the only way to handle this is to try other potential start areas, but we are studying this problem.

Another current study concerns the way to constraint even more the process, either to respect a need from radiologists to impose a specific entry zone, or to avoid scenarios impossible to reproduce by radiologists (for example, a needle that would be parallel to the body, as shown on figure 8(a)). For the first case, we added a functionality to the system that allows the radiologist to draw an "insertion window" on the skin (figure 8(b)), and that forces the system to discover the optimal result within the selected area. This also has the advantage to reduce the field of possible results, and to speed up the process. This could also be done automatically: the system could compute all possible insertion zones, for instance using a ray-tracing-based algorithm, and eliminate some of them according to predefined criteria. This subject is currently being singled out.

For the second case, in a first idea we chose to impose one restriction to the trajectory: it has to cross the skin. That way, we will never obtain such an impossible result. However, it may sometimes be too restrictive: for instance if the scan data contains only a few slices, concerning a small portion of the abdomen, a whole interval of solutions (orientations) may be forgotten. This point is also being studied.

6. Enhancing the simulator with virtual reality and haptics

Obviously, visualizing a 3D scene on a 2D screen and manipulating it using a mouse may not be very intuitive and efficient. The user can only visualize a 2D projection of the reconstructed patient, and often has to rotate it to appreciate the volumic information. In the same way, positioning a needle with the mouse may be tedious, as aligning it on the 2D projection is quite easy, but the lack of depth information makes it necessary to rotate the patient's meshes in order to place it correctly according to the third direction. That is why we experimented the use of virtual reality and haptics to enhance visualization and manipulation during simulation and planning processes, expecting a great benefit for our tool.

6.1 *Virtual reality*

The virtual reality display device we used in our experiments is a 2-screen Consul workbench from Barco with tracked shutter glasses. To interact with this device, we tried 2 different peripherals: a tracked 5DT Data Glove 5, and a 6 degree of freedom wireless Flystick from A.R.T.

6.1.1 Display. The workbench allows the representation of 3D objects in space. To simulate the volumic effect, the device sends different information to each eye via shutter glasses, that dispense images alternatively. Thanks to the stereoscopic effect, the brain recreates the image of a floating 3D object. When coupled with a tracking device on the top of the glasses, the system recalculates the 3D scene according to the position of the user.

This technique gives us the benefit of a realistic visualization of the 3D reconstructed patient (figure 9). The physician can view his patient as if he really was in front of him, with the real size, and he can turn his head around the body to find a better angle of view. Moreover, he can take advantage of all the software possibilities, that means that he can see through organs by making them transparent, and he can simulate realistically or plan an operation.

We had this kind of device at our disposal in the laboratory, and it proved its usefulness and convenience compared to 2D screens for our type of application. But other 3D visualization devices could be also used, such as the Reachin Display from Reachin Technologies AB, that is coupled with a haptic device. However, the workbench
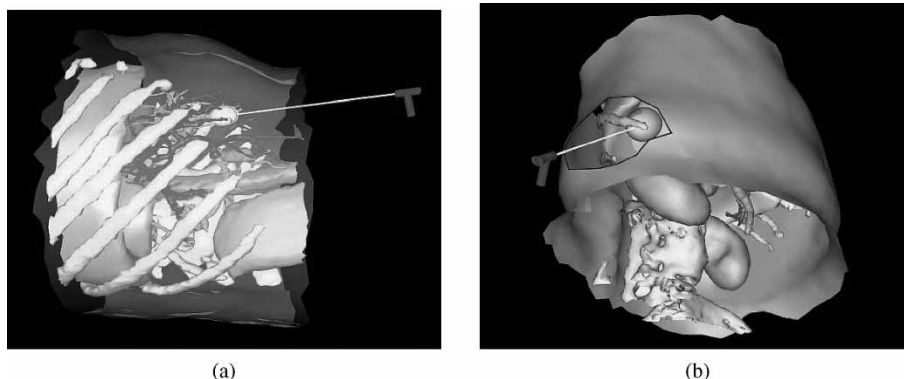

(a)   (b)

Figure 8. Reduction of the search area to overcome unfeasibilities. (a) Trajectory impossible to reproduce in practice and (b) Restriction of the search within a predefined window.
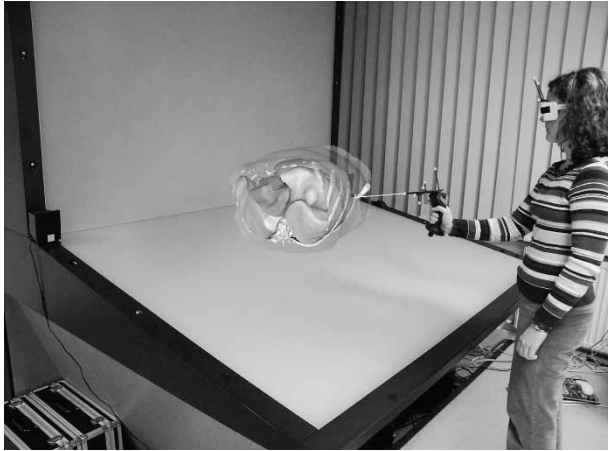
Figure 9. Simulation displayed on a 2-screen workbench, with a flystick as an interaction peripheral.

has the advantage to display an image of the patient that is in real size, giving a greater impression of realism, very beneficial for training.

6.1.2 Simple interaction. To complement this 3D visualization, we had to find an adequate interaction device. On a first idea, we decided to experiment two different types of common VR interaction devices. The first one, the Data Glove, consists in a sensitive glove using fiber optic technology, that ensures the measurement of the flexure of fingers, and the orientation (pitch and roll) of the user's hand. Interaction events are generated when the hand takes a particular position. Our idea was to allow the manipulation of a virtual needle by simulating the hold of the needle with the hand wearing the Data Glove. When the user pinches the thumb and forefinger, he can catch the probe. Then every movement of the hand is sent back to the system that reflects it on the position of the virtual needle in real time. The Data Glove also allows to manipulate the scene, by applying directly to the scene the movements of the hand. This technique is realistic, but we found it not precise enough to be used in a medical application.

That is why we experimented another peripheral: the 6 degree of freedom flystick, a kind of 3D joystick. Its movements (translations and rotations) are captured thanks to an optical tracking. On a first attempt, we decided to represent the virtual needle on screen as being the continuation of the flystick, as shown of figure 9. This was very realistic, but had a drawback: if you manipulated the needle with the flystick, then fixed the position of the needle in order to use the flystick to manipulate the 3D scene, and then you wanted to move again the needle, the virtual representation of the probe "jumped" to the actual position of the flystick, that could confuse the user. For that reason we decided to consider the flystick as a virtual hand manipulator, that can go and catch the needle tip when needed, as it would be the case with a real hand. That way, we avoid unwanted moves of the probe. Compared to

the Data Glove, the flystick is more precise, and gives the benefit of its set of buttons, that lets the user easily interact with the application, switch between manipulation modes, set organs transparencies, and handle all other features.

Nevertheless, even if both of these interaction peripherals are well designed for virtual reality and even if they allow an intuitive navigation and manipulation, we had to conclude that none of these attempts were convincing for a realistic surgical training tool, as they do not offer any haptic sensation. As our goal was to provide a performing and realistic simulation and training tool, we also decided to redirect our investigations towards haptic devices, as explained in the following section.

6.2 Haptic devices

We used for our haptic experiments two kinds of Phantom devices from Sensable technologies: a Phantom Desktop 3dof, and a Phantom Premium 6dof. These devices consist in an articulated arm with position sensors that captures the motion of a stylus, and that ensures force feedback thanks to small motors located in the hinges. Both Phantom devices have 6 degrees of freedom in input, that means that it can acquire all translations and rotations performed on the stylus. The difference between them is in the force feedback output. The Phantom Desktop 3dof only renders translational forces, whereas the Phantom Premium 6dof also controls the rotation of the stylus.

Because the Phantoms usually are small and static devices, with a socle that has to lay on a table, and also because we wanted to quantify the benefits of the use of these devices without the intervention of other enhancements of any kind, we experimented it with a 2D view on a classic desktop screen, as shown on figure 10.

These Phantom arms also allows a friendly manipulation of the patient view. The force feedback allows the user to feel realistic sensations such as resistance and friction forces due to needle insertion through the skin or other organs, or the locking of direction of the needle when it is yet inserted. The realistic rendering of mechanical forces is an important point for the training of surgeons, especially when you know that training increases the quality of the results of this treatment, as demonstrated in (Poon *et al.* 2004). We think that a realistic haptic simulation brings a better experience than a simple visual experiment.

For this experiment, we chose to simulate directly the probe with the stylus of the Phantom. The user holds the stylus as if he was holding the needle. The feedback forces are applied to the stylus and are felt as if there was a resistance of the patient's body when inserting the needle.

6.2.1 Forces during needle insertion. Let us describe briefly the different phases of the insertion of a needle that imply a force feedback. First, there is a surface contact phase, where the needle tip is in contact with the surface of the tissue but is not yet inserted. And secondly, there is a

Figure 10. Simulation using Phantom Premium 6dof haptic device.

penetration phase, where friction forces are involved. For these forces computations, we did not choose a finite elements approach as it is sometimes done in the literature, that would be more precise but slower.

When the needle tip has not penetrated yet into the tissue, it can either be in static contact with it, or slide on it. If there is a static contact, pushing the needle leads to a deformation of the tissue, that will be discussed in Section 6.2.3, and to a force feedback of the surface. We consider that the needle tip imposes the displacement of a vertex of the mesh, the contact point, bringing it to a position T. The distance r between T and the rest position P_o of the contact point will give us the force f_e submitted back to the needle tip by the Phantom: $\vec{F} = f_e = -k\,r u_r$, where k is the coefficient of elasticity characterizing the tissue (figure 11(a)).

If the needle goes "backwards", the tip can slide over the surface. In this case, point P_o is updated and becomes a virtual equilibrium point. In this sliding mode, occurring when the projection of f_e on the surface exceeds a threshold F_G, the force submitted to the needle tip becomes $\vec{F} = f_{e_N} - k r_G u_H$, where f_{e_N} is the normal component of f_e, neeessary to avoid needle insertion into the tissue, u_H is the unit vector along the line passing through P_o and the perpendicular projection of T on the surface, and r_G is a parameter depending on the characteristics of the probe, of the tissue, and on the pressure on the surface (figure 11(b)).

In parallel to the works on RF simulation, we deviated this sliding mode from its initial objective to adapt it to another functionality: by simply artificially increasing the threshold necessary to pierce the skin, we can obtain a "palpation mode". This mode allows the user to feel the bones through the skin while sliding on it, as if he was palpating the area with his finger. This functionality is useful when the operator needs to feel the bones to seek the right insertion location, for instance the ribs for RF, or the vertebrae for an application on peridural anesthesia (figure 12(c)).

When the force necessary to pierce the tissue is reached, the needle starts its penetration. We suppose that the direction of the needle does not change once the penetration has begun, as it will be discussed in Section 6.2.2.

As it was already determined, (e.g. in DiMaio and Salcudean 2002), two forces can be distinguished: a linear friction force, supposed to be homogeneously distributed along the needle, and a force at the needle tip. In view of the quite slow displacements submitted to the probe, we chose to describe the mechanical behavior as a function of the displacement. The two forces cited above will both be modeled by elastoplastic models. This mechanical modelization puts into play elasticity coefficients, that depends on the type of tissue. We used the results of the studies of Maurin *et al.* (2004).

All of these forces are computed in real-time with respect to haptics (1 kHz), in order to have a satisfying response of the device.

6.2.2 Locking needle direction. As we said earlier, we chose to consider that once the needle in inserted into the body, it is forbidden to rotate the needle. That is why we had to impose the direction of the needle during the penetration, and to allow only a translation of the probe following the direction detected at the moment of the introduction.

Simulating this restriction is quite easy with the Phantom Premium 6dof, that allows a control over the rotation of the stylus. To simulate it with the Phantom Desktop 3dof that does not include this feature, we chose to use the "haptic illusion" or "pseudo-haptic feedback" effect, detailed by Lecuyer *et al.* (2001). It relies on an optimal combination of the visual feedback and the actions of the user on the virtual environment. It is possible to generate some haptic sensations only with visual feedback. The visual perception
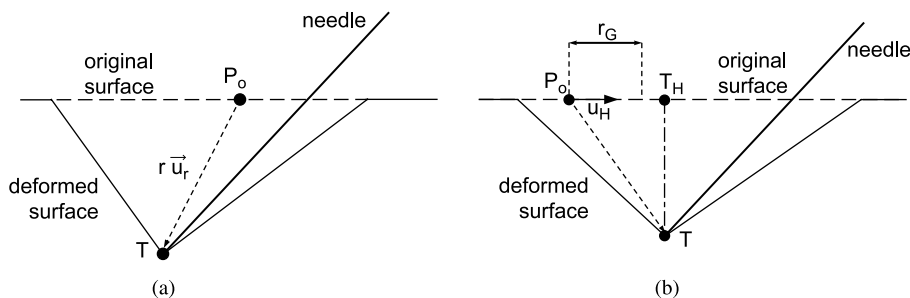

Figure 11. Determining of the forces before tissue penetration. (a) Needle moves forward: static contact mode and (b) Needle moves backwards: sliding contact mode.

(b) deformed mesh

(c) palpation mode

(a) deformation during the penetration of the needle within the skin
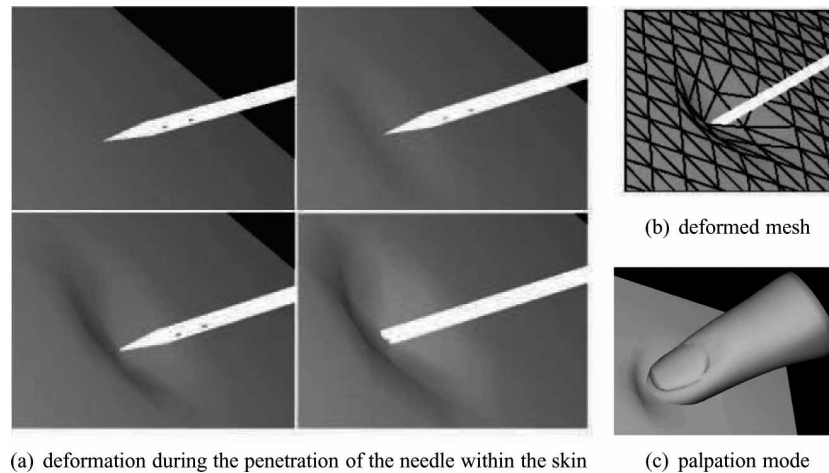
Figure 12.   Results of the deformation of the skin during the penetration of the needle or palpation. (a) deformation during the penetration of the needle within the skin (b) deformed mesh (c) palpation mode.

of a locked direction of the needle creates a haptic illusion of a really locked direction of the stylus, so that users nearly do not rotate the stylus when this rotation does not affect the virtual needle on the screen.

This haptic illusion also allows us to overcome a technical problem: the maximum stiffness of the Phantom is not sufficient to render properly the contact with rigid objects. In our case, the realism of the contact between the needle and a bone is hard to obtain, as it is impossible to block completely and firmly the arm of the Phantom. That is why we chose to use a haptic illusion to enhance this realism: we affect the perception of stiffness by visually forbidding the penetration of the needle into the bone. That way, even if the contact does not seem hard enough with the Phantom, it is reinforced and sensed as firm when it is visually firm.

6.2.3 Deformation of the tissues. The predominance of visual information over haptic information leaded us to enhance the haptic feedback with deformations of the tissues. We focus on visible deformations, i.e. of the skin surface. The deformation occurs as soon as the needle tip touches the surface.
We perform a quite simple deformation, following the stylus location for the contact point, and that affects not only the contact point but also all points located within a spherical influence volume. The farthest these additional points are from the contact point, the less they are displaced. An extrusion function determines the relationship between distance from the contact point and displacement induced by the deformation. We chose not to perform any local remising, as for our particular case of skin perforation the deformation is quite homogenous, and we observed that a simple smoothing of the surface was realistic enough, as can be seen on figure 12.

When the needle pierces the skin, the way of computing the deformation remains the same, but the contact point is not linked with the position of the needle tip anymore, but follows the point of the probe that is located at the penetration point. We can see on figure 12 the results of

the visual deformation of the skin, for both phases of perforation, and for palpation mode.

6.2.4 Reports. We asked to a set of 15 unexperimented users to try the simulator with the Phantom: 5 were surgeons and 10 were not, none of the 15 had used this application before.
All of them reported that the haptic sensation greatly enhanced the simulator. All of them also reported that the visual deformation of the skin improved the realism of the simulation, because it underlined the location of the puncture, and the force applied with the needle, providing a useful additional feedback.

However, most of them regretted the lack of visual feedback when moving the needle in the 3D scene around the patient, bringing it towards the skin. It often took several attempts to reach an aimed target point. We concluded that the application would benefit from a visual accentuation of the depth information for the needle. We are currently working on this problem, that will certainly be solved with the use of a shadow. However, this kind of problem would probably be less noticeable with a VR display device.

6.3 Discussion

The various experiments we made with virtual and haptic devices confirmed an effective enhancement of realism of the simulation tool. The use of the Phantom obtained a unanimous favorable opinion, as well as the 3D visualization with the workbench, convincing us to go further. But for now, each one of these devices can only be used alone: you can have either the VR display or the force feedback. Conjugating both functionalities would be appreciated, for instance, by using a specific display such as the Reachin display we already mentioned earlier. But this device would have the drawback to offer only a small representation of the patient. To keep the real size property, it becomes manifest that a haptic feedback in conjunction with the workbench would be the best solution.

We considered adapting the Phantom for a use with the workbench. But firstly it would impose to put it on a

special stand, preferably adjustable in position and height. And secondly, it would have involved problems of range of motion, and of relative size if the user zooms in or out. It would probably have imposed a use as an indirect peripheral, and the user would not have been able to act directly on the patient's view, but only within the range of motion of the Phantom. From that point of view, it would have decreased the realism of any simulation. But maybe we could imagine to use a bigger device having a large range of motion covering the whole workbench workspace, in the way of the Grope from UNC for instance, or a large configuration of the Spidar.

7. Conclusion

We presented in this paper a first version of a realistic RFA simulation and treatment planning tool. The experiments confirmed the feasibility of RFA modeling, simulation, and automatic planning. They also confirmed the relevance of the use of virtual reality and haptic tools to enhance the realism of such a tool. The real-time deformation of the necrosis shape according to local vessels positions, and the automatic placement of the needle with respect to surrounding organs will improve strategic planning and prediction of treatments results. The tool *RF-Sim* also aims to be used for training of novice surgeons, to help them in comparing their strategy proposal to an optimal needle position that would be proposed by the system, and to acquire faster some experience in this type of operation.

However, in the future we plan to improve efficiency of the algorithms to speed up the planning process and to have a more robust tool able to treat even the most difficult and specific cases. We also plan to enhance our tool by including extra radiologic information to increase realism even more.

The use of haptic devices to simulate the force feedback when inserting the needle, and of a virtual reality display system, in order to provide the user with a quality immersive impression, reinforces the sensation of realism. Separate experiments of manipulation with a workbench and with a Phantom, including organs deformations and force feedback, already gave very promising results. We are currently following through this project to find the best combination between display and interaction peripherals, in order to be able to propose an optimal tool in terms of realism and performance.

Acknowledgements

References

G. Antoch, H. Kuehl, F. Vogt, J. Debatin and J. Stattaus, "Value of CT volume imaging for optimal placement of radiofrequency ablation probes in liver lesions", *J. Vasc. Interv. Radiol.*, 13, pp. 1155–1161, 2002.

T. Butz, S.K. Warfield, K. Tuncali, S.G. Silverman, E. van Sonnenberg, F.A. Jolesz and R. Kikinis, "Pre- and intra-operative planning and simulation of percutaneous tumor ablation", *Lect. Notes Comp. Sci.*, 1935, pp. 317–326, 2000.

B. Cady, R.L. Jenkins, G.D. Steele, W.D. Lewis, M.D. Stone, W.V. McDermott, J.M. Jessup, A. Bothe, P. Lalor, E.J. Lovett, P. Lavin and D.C. Linehan, "Surgical margin in hepatic resection for colorectal metastasis: a critical and improvable determinant of outcome", *Ann. Surg.*, 227, pp. 566–571, 1998.

M.H. Chen, W. Yang, K. Yan, M.W. Zou, L. Solbiati, J.B. Liu and Y. Dai, "Large liver tumors: protocol for radiofrequency ablation and its clinical application in 110 patients—mathematic model, overlapping mode, and electrode placement process", *Radiology*, 232, pp. 260–271, 2004.

T. de Baere, A. Denys, B.J. Wood, N. Lassau, M. Kardache, V. Vilgrain, Y. Menu and A. Roche, "Radiofrequency liver ablation: experimental comparative study of water-cooled versus expandable systems", *Am. J. Roentgenol.*, 176, pp. 187–192, 2001.

T. de Baere, B. Bessoud, C. Dromain, M. Ducreux, V. Boige, N. Lassau, T. Smarya, B.V. Girish, A. Roche and D. Elias, "Percutaneous radiofrequency ablation of hepatic tumors during temporary venous occlusion", *Am. J. Roentgenol.*, 176, pp. 187–192, 2002.

S.P. DiMaio and S.E. Salcudean, "Needle insertion modelling for the interactive simulation of percutaneous procedures", *Lect. Notes Comp. Sci.*, 2489, pp. 253–260, 2002.

G.D. Dodd, III, M.S. Frank, M. Aribandi, S. Chopra and K.N. Chintapalli, "Radiofrequency thermal ablation: computer analysis of the size of the thermal injury created by overlapping ablations", *Am. J. Roentgenol.*, 177, pp. 777–782, 2001.

S.N. Goldberg, "Radiofrequency tumor ablation: principles and techniques", *Eur. J. Ultrasound*, 13, pp. 129–147, 2001.

S.N. Goldberg, G.S. Gazelle and P.R. Mueller, "Thermal ablation therapy for focal malignancy: a unified approach to underlying principles techniques, and diagnostic imaging guidance", *Am. J. Roentgenol.*, 174, pp. 323–331, 2000.

J. Gopalakrishnan, "A mathematical model for irrigated epicardial radiofrequency ablation", *Ann. Biomed. Eng.*, 30, pp. 884–893, 2002.

M.K. Jain and P.D. Wolf, "A three-dimensional finite element model of radiofrequency ablation with blood flow and its experimental validation", *Ann. Biomed. Eng.*, 28, pp. 1075–1084, 2000.

A. Lecuyer, J.M. Burkhardt, S. Coquillart and P. Coiffet, "Boundary of illusion: an experiment of sensory integration with a pseudo-haptic system", *IEEE VR*, pp. 115–122, 2001.

T. Livraghi, S.N. Goldberg, S. Lazzaroni, F. Meloni, L. Solbiati and G.S. Gazelle, "Small hepatocellular carcinoma: treatment with radio-frequency ablation versus ethanol injection", *Radiology*, 210, pp. 655–661, 1999.

J.P. McGahan and G.D. Dodd, III, "Radiofrequency ablation of the liver: current status", *Am. J. Roentgenol.*, 176, pp. 3–16, 2001.

B. Maurin, J. Gangloff, B. Bayle, M. de Mathelin, O. Piccin, P. Zanne, C. Doignon, L. Soler and A. Gangi, "A parallel robotic system with force sensors for percutaneous procedures under CT-guidance", *Lect. Notes Comp. Sci.*, 3217, pp. 176–183, 2004.

A. Meijster, J.B.T.M. Roerdink and W.H. Hesselink, "A general algorithm for computing distance transforms in linear time", *Mathematical Morphology and its Applications to Image and Signal Processing*, J. Goutsias, L. Vincent and D. S. Bloomberg, Eds., Boston, MA: Kluwer Academic, pp. 331–340, 2000.

P.L. Pereira, J. Trübenbach, M. Schenck, J. Subke, S. Kroaber, I. Schaefer, C.T. Remy, D. Schmidt, J. Brieger and C.D. Claussen, "Radio-frequency ablation: *in vivo* comparison of four commercially available devices in pig livers", *Radiology*, 232, pp. 482–490, 2004.

R.T. Poon, K.K. Ng, C.M. Lam, V. Ai, J. Yuen, S.T. Fan and J. Wong, "Learning curve for radiofrequency ablation of liver tumors: prospective analysis of initial 100 patients in a tertiary institution", *Ann. Surg.*, 239, pp. 441–449, 2004.

[§]Equipe-Projet Multi-Laboratoires Imagerie et Robotique Médicale et Chirurgicale; http://irmc.u-strasbg.fr/.

W.H. Press, S.A. Teukolsky, W.T. Vetterling and B.P. Flannery, *Numerical Recipes in C++: The Art of Scientific Computing*, 2nd ed., New York, NY: Cambridge University Press, 2002.

J.C. Rewcastle, G.A. Sandison, K. Muldrew, J.C. Saliken and B.J. Donnelly, "A model for the time dependent three-dimensional thermal distribution within iceballs surrounding multiple cryoprobes", *Med. Phys.*, 28, pp. 1125–1137, 2001.

S. Rossi, F. Garbagnati, R. Lencioni, H.P. Allgaier, A. Marchiano, F. Fornari, P. Quaretti, G. Di Tolla, C. Ambrosi, V. Mazzaferro, H.E. Blum and C. Bartolozzi, "Percutaneous radio-frequency thermal ablation of nonresectable hepatocellular carcinoma after occlusion of tumor blood supply", *Radiology*, 217, pp. 119–126, 2000.

L. Soler, H. Delingette, G. Malandain, J. Montagnat, N. Ayache, C. Koehl, O. Dourthe, B. Malassagne, M. Smith, D. Mutter and J. Marescaux, "Fully automatic anatomical, pathological, and functional segmentation from CT scans for hepatic surgery", *Comp. Aided Surg.*, 6, pp. 131–142, 2001.

S. Tungjitkusolmun, S. Staelin, D. Haemmerich, J.Z. Tsai, J.G. Webster, F.T. Lee, D.M. Mahvi and V.R. Vorperian, "Three-dimensional finite element analyses for radio-frequency hepatic tumor ablation", *IEEE Trans. Biomed. Eng.*, 49, pp. 3–9, 2002.

C. Villard, L. Soler, N. Papier, V. Agnus, S. Thery, A. Gangi, D. Mutter and J. Marescaux, "Virtual radiofrequency ablation of liver tumors", *Lect. Notes Comp. Sci.*, 2673, pp. 366–374, 2003.

T.F. Wood, M. Rose, M. Chung, D.P. Allegra, L.J. Foshag and A.J. Bilchik, "Radiofrequency ablation of 231 unresectable hepatic tumors: indications, limitations, and complications", *Ann. Surg. Oncol.*, 7, pp. 593–600, 2000.

T. Yamasaki, F. Kurokawa, H. Shirahashi, N. Kusano, K. Hironaka and K. Okita, "Percutaneous radiofrequency ablation therapy for patients with hepatocellular carcinoma during occlusion of hepatic blood flow: comparison with standard percutaneous radiofrequency ablation therapy", *Cancer*, 95, pp. 2353–2360, 2002.